Laser-driven collisionless shock acceleration of protons from gas jets tailored by one or two nanosecond beams

J Bonvalet, P Loiseau, J.-R Marquès, E Atukpor, E d'Humières, J Domange, P Forestier-Colleoni, F Hannachi, L Lancia, D Raffestin, et al.

Physics of Plasmas

Laser-driven collisionless shock acceleration of protons from gas jets tailored by one or two nanosecond beams

Cite as: Phys. Plasmas **28**, 113102 (2021); https://doi.org/10.1063/5.0062503
Submitted: 06 July 2021 • Accepted: 11 October 2021 • Published Online: 02 November 2021

J. Bonvalet, P. Loiseau, J.-R. Marquès, et al.

Physics of Plasmas ARTICLE scitation.org/journal/php

Laser-driven collisionless shock acceleration of protons from gas jets tailored by one or two nanosecond beams

Cite as: Phys. Plasmas **28**, 113102 (2021); doi: 10.1063/5.0062503
Submitted: 6 July 2021 · Accepted: 11 October 2021 ·
Published Online: 2 November 2021

J. Bonvalet,[1,a)] P. Loiseau,[2,3] J.-R. Marquès,[4] E. Atukpor,[5] E. d'Humières,[1] J. Domange,[5] P. Forestier-Colleoni,[4] F. Hannachi,[5] L. Lancia,[4] D. Raffestin,[1] M. Tarisien,[5] V. Tikhonchuk,[1,6] and Ph. Nicolaï[1]

AFFILIATIONS

[1]Université Bordeaux-CNRS-CEA, CELIA, UMR5107, Talence, France
[2]CEA, DAM, DIF, F-91297 Arpajon, France
[3]Université Paris-Saclay, CEA, LMCE, 91680 Bruyères-le-Châtel, France
[4]LULI, CNRS, École Polytechnique, CEA, Sorbonne Université, Institut Polytechnique de Paris, F-91128 Palaiseau Cedex, France
[5]Université Bordeaux, CNRS-IN2P3, CENBG F-33175 Gradignan, France
[6]ELI-Beamlines Center, Institute of Physics, Czech Academy of Sciences, Za Radnici 835, 25241 Dolní Břežany, Czech Republic

[a)]**Author to whom correspondence should be addressed:** julien.bonvalet@u-bordeaux.fr

ABSTRACT

It was proposed recently that laser-ion acceleration in gas jets may be significantly improved if each side of a gas jet target is tailored by an auxiliary nanosecond laser pulse [Marquès *et al.*, Phys. Plasmas **28**, 023103 (2021)]. In the present study, the proton acceleration by electrostatic shock in these one- or two-side tailored plasmas is investigated using particle-in-cell simulations. It is demonstrated that the formation of a thin plasma layer with a steep density profile and a maximum density of the order of the critical density strongly improves the proton acceleration in the forward direction with a maximum ion energy of tens of MeV with mildly relativistic laser pulses. Proton acceleration up to tens of MeV is predicted using realistic plasma density profiles obtained from tailored gas jet targets compared to a few MeV reported in other publications.

I. INTRODUCTION

Over the past decade, laser-accelerated ion beams have attracted considerable interest due to their promising characteristics for many potential applications, such as particle physics,[2,3] proton radiography,[4,5] cancer therapy,[6,7] and isotope production.[8] These applications require ion beams with controllable energy bandwidth, low divergence at the source, and a high repetition rate.

Several regimes have been proposed for laser-driven ion acceleration: Target Normal Sheath Acceleration (TNSA),[9,10] Radiation Pressure Acceleration (RPA),[11–14] Breakout Afterburner Acceleration (BOA),[15,16] and Collisionless Shock Acceleration (CSA). Among these regimes, CSA has become a very attractive candidate for the generation of high quality ion beams using gas jets as it eliminates the constraints of target replacement and realignment between the consecutive shots and reduces the amount of debris. Moreover, compared to the other mechanisms, protons accelerated in electrostatic shocks have significant advantages in terms of low divergence and low energy spread: the shock wave front can accelerate upstream ions by reflecting them to twice the shock velocity[17] when the kinetic energy of incoming ions is less than the shock potential in the shock-rest frame.

Several numerical studies[18,19] predict the possibility to obtain high-quality quasi-monoenergetic ion beams by the CSA mechanism, with energies up to a hundred of MeV, but impose severe requirements on the target, especially on the scale length of the plasma profile that strongly influences the quality of the accelerated particles. Until now, experiments[20–26] have not succeeded to accelerate ions above a few MeV, neither by using gas targets nor exploded solid targets. This experimental limit on ion energy can be explained by the fact that the laser beam undergoes non-linear modifications during its propagation

in the low density region at the entrance of the plasma and cannot launch an efficient electrostatic shock.

In this study, we demonstrate numerically the possibility to accelerate protons to several tens of MeV by optimizing the hydrogen gas jet profile. To achieve this goal, and as proposed in Marques *et al.*,[1] one or two nanosecond laser beams propagating perpendicularly to the main ps laser pulse through the low-density edge of the gas jet are used to shape the plasma density profile. In this paper, a numerical chain formed by the hydrodynamic code TROLL[27] and the Particle-In-Cell (PIC) code SMILEI[28] is used to analyze and optimize the physical processes of gas profile tailoring and proton acceleration. Under the best conditions, protons can be accelerated to energies of several tens of MeV in the shock. Depending on the number of ns-laser beams used to shape the plasma profile, at the front side or both at the front and rear sides, this acceleration scheme allows to reach proton energies up to 60 MeV with an energy spread of ≈14% and a number of 10^{10} protons per steradian.

This paper is organized as follows. In Sec. II, the theoretical model of shock acceleration in near critical plasmas is reminded and supported by PIC simulations to highlight the parasitic processes operating in the gas wings of a supersonic gas target: laser beam self-focusing and filamentation that deteriorate the laser pulse before the shock formation. In Secs. III and IV, the principle of the laser tailoring scheme is presented. We explain how it allows us to solve the issues described in Sec. II and improves the shock acceleration in gas targets. In Sec. V, an optimization of the shock acceleration scheme is performed through the variation of parameters of the density profiles. Section VI summarizes the main results of this study.

II. ION ACCELERATION IN DENSE GAS TARGET

A. Laser-driven electrostatic shocks in near-critical density plasmas

CSA is based on the formation of an electrostatic shock that is typically associated with the excitation of ion acoustic waves. The formation of a collisionless electrostatic shock requires the creation of a localized region of higher pressure within a plasma with electron temperature T_e much larger than the ion temperature T_i.[17,18] As this region of high pressure (defined as the downstream region) expands, it can drive a shock wave into the surrounding lower-pressure plasma (defined as the upstream region). The interaction of a high-intensity laser with a near-critical density plasma can efficiently produce these conditions in two ways:

- If the plasma remains opaque to the laser, the radiation pressure drives a density steepening in the region irradiated by the laser, and this density steepened plasma front surface is accelerated as a moving piston and creates the pressure discontinuity necessary for shock formation.[18]
- If the plasma is transparent to the laser, electrons are heated by the laser to MeV-level energies and drive a density breakout at the descending density profile.

An efficient plasma heating is the key factor in CSA. In contrast to RPA, to drive an efficient electrostatic shock, the laser has to heat the entire plasma in volume and create a uniform temperature distribution. To obtain such a uniform temperature profile, the target thickness has to be limited to allow the electrons recirculation in the target.[17] This condition reads $L_t < \lambda_0 (m_i/m_e)^{1/2}$, where L_t is the target thickness, λ_0 is the laser wavelength, and m_i (m_e) is the ion (electron) mass. This condition limits the target thickness by 50–100 μm for the laser wavelength of 1 μm, assuming the density is close to the critical density. The use of a supersonic gas jet allows us to reach this near critical density condition but is inconsistent with the requirement on the target thickness since the typical size of a gas jet is of a several millimeters.

This study is based on a method of creation of thin plasma layers that satisfy this size requirement despite a spatially extended initial profile.

Once created, the shock wave propagates with a velocity defined as $v_{sh} = MC_s = M\sqrt{ZT_e/m_i}$ where M is the Mach number, C_s the local sound speed, and Z the ion atomic number. Thus, the shock velocity depends directly upon the electron temperature, indicating that to reach high velocities, the plasma has to be strongly heated. This gives the first constraint on the ion energy in CSA: $E_i \propto m_i C_s^2 = ZT_e$; therefore, in order to reach MeV-level ion energies, the electron temperature has to also be ∼1 MeV. A theory of collisionless electrostatic shocks based on the Sagdeev pseudo-potential method shows that in isothermal Boltzmann plasmas, only a Mach number $M > 1.6$ leads to a strong shock creation where ions can be reflected.[29] The charge separation occurs at the moving front, generating strong electric fields which can reflect the incoming ions. Considering a frame moving with the shock, in which the shock is stationary and upstream ions are impinging upon it at the shock velocity, these ions will climb the potential until they are either stopped or pass over the barrier and through the shock front. The reflection condition is therefore that the electrostatic potential barrier exceeds the ion kinetic energy: $e\Phi_{sh} > 1/2 m_i v_i^2$. If this condition is verified, the ion is stopped and accelerated down the potential. Its final velocity equals to minus its initial speed in the shock reference frame. In the lab frame, if the particle starts at rest, the reflected ion moves at $v_i \approx 2v_{sh}$. Since the acceleration process in the shock front for the highest energy ions is determined only by the shock velocity, which remains approximately constant, it is expected that an experimental signature for this mechanism can be seen as peaked structures in the ion energy distribution. The more the shock velocity is uniform, the more the reflected ion energy distribution is narrow. While a high reflection efficiency is desirable in order to accelerate a large number of ions, it could have a deleterious effect on the shock structure with a strong dissipation, leading to decreasing its velocity and thus spreading the ion energy distribution.[30] For a more realistic case where the upstream plasma is expanding at some velocity v_0, the relative motion between the shock and the particle needs to be taken into account and the reflected ions move at $v_i \approx 2v_{sh} - v_0$.

Figure 1 summarizes the important steps for an efficient ion acceleration by a laser-driven electrostatic shock as a function of the laser beam propagation direction as follows:[31–33]

(1) The laser beam has to keep its integrity propagating in the gas density ramp in order to transfer a maximum of its energy to the plasma in the higher density region.
(2) As the laser pulse reaches the high density region, the absorption has to be efficient. In order to create a strong shock, the peak plasma density must be on the order of the relativistic critical density[18] $n_e \cong \gamma n_c$, where $\gamma = \sqrt{1 + a_0^2/2}$, and a_0 is the normalized laser vector potential. The thickness of the high

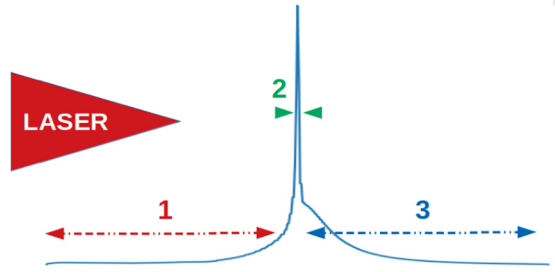

FIG. 1. Optimized gas density profile needed for efficient ion acceleration by laser-driven electrostatic shock: (1) A low density pedestal to avoid that the laser undergoes filamentation, self-focusing, and Raman scattering, and loses a large part of its energy. (2) A narrow high density region with the maximum density close to the relativistic critical density (γn_c) is used to produce a strong shock. (3) An upstream region crossed by the shock should present a smooth density profile to avoid TNSA competition. The typical widths of these three layers are of several tens of micrometers for layers (1) and (3) and thinner (several micrometers) for layer (2).

density region has to allow an efficient absorption of laser pulse energy.

(3) The upstream region crossed by the shock plays a crucial role in the ion energy distribution. Because of a finite size of the plasma layer, expansion of hot electrons into vacuum gives rise to a non-uniform electrostatic field in the sheath and introduces a spread in ion velocities, broadening the ion energy distribution as typical of TNSA. This sheath field can be controlled by using an extended upstream plasma density profile. For an exponential plasma profile with a scale length L_g, the sheath electric field is constant at early times ($t \ll 4L_g/C_s$)[34] before wave breaking, and its amplitude given by $E_{TNSA} = T_e/eL_g$ can be tuned by choosing the length L_g. The necessary condition for the generation of monoenergetic ion beams[18] can be written as $L_g \gg 2\lambda_D$, where λ_D is the Debye length, on the order of a few micrometers for a MeV-level temperature in this region. The final ion energy distribution can finally be broadened by the initial ion velocity distribution before their reflection by the shock but especially by a shock velocity that decreases in time while the shock slows down in the upstream region where the temperature is not uniform.

This last requirement on the length of the plasma density profile of the rear side of the target ($L_g \gg 2\lambda_D$) seems to run contrary to the requirement on the target thickness ($L_t < \lambda_0(m_i/m_e)^{1/2}$); however, since L_g is on the order of few micrometers and L_t on the order of a hundred micrometers, these two conditions can be satisfied in our tailoring plasma scheme.

In order to study laser-ion acceleration with unshaped or shaped gas jets, we performed 2D planar particle-in-cell simulations using the code SMILEI.[28] The simulation box is 1 mm long and 60 μm wide, resolved with 20 000 × 800 cells with 50 particles per cell. The total simulation time is 20 ps, sampled with a time step of $\Delta t = 0.06$ fs. At each simulation boundary, absorbing conditions are adopted for both particles and fields, and the laser is launched from the left side with electric field in the simulation plane. The laser parameters correspond to the PICO2000 laser at LULI, France.[1] They are a Gaussian beam of wavelength of 1 μm with a temporal envelope of 1.0 ps at full width at half maximum (FWHM) and a spot of 10 μm at FWHM, focused at the center of the simulation box. The Rayleigh length is on the order of a millimeter. The maximum laser intensity of 5.0×10^{19} W cm^{-2}, corresponding to a normalized laser vector potential of 6, reaches the center of the gas jet ($x = 500$ μm) at $t = 2.5$ ps from the beginning of the simulation. The particle diagnostic records the accelerated protons at the limits of the simulation box ($x = 0$, $x = 1$ mm, $y = 0$ and $y = 60$ μm).

B. Laser energy losses in the rising density ramp of a gas jet target

In previous numerical studies,[18,22,35] the plasma density profile was optimized in terms of laser absorption and shock formation with a 10 μm linear ramp at the front side and an exponential slope at the rear side with a scale length $L_p = 20$ μm. However, the gas jets used in experiments have a much broader density profile. Then, the first issue preventing an efficient ion acceleration in an electrostatic shock is the development of non-linear phenomena (self-channeling, filamentation, Raman scattering) that occur during the laser propagation in the gas density ramp.

The plasma profile, used in this PIC simulation, is shown in Fig. 2. It corresponds to a supersonic hydrogen gas jet used by Puyuelo-Valdes *et al.*,[23] with a Lorentzian radial profile $n_{e0}(r) = n_0/(1 + [r/r_0]^2)$, where $r_0 = 70$ μm. The orange arrow represents the main laser beam direction. The laser has to cross a gas density from 1×10^{19} to 1×10^{21} cm^{-3} over several hundred micrometers and may lose a large part of its energy due to non-linear phenomena like filamentation and self-channeling. In a recent experiment by Puyuelo-Valdes *et al.*[23] with such a gas jet, an isotropic acceleration with a flux of 10^{11} protons/MeV/sr was measured at low energies up to 2–3 MeV, and secondary peaked structures were observed between 3 and 5 MeV at 0°, 30°, 70°, and 90°, respectively.

The excitation of the filamentation instability breaks the laser beam before it can reach the peak of the density profile and results in proton acceleration mainly at the beginning of laser propagation. As illustrated in Fig. 3(a), the laser pulse loses its integrity and splits in multiple filaments, crossing the wings of the gas where the density is

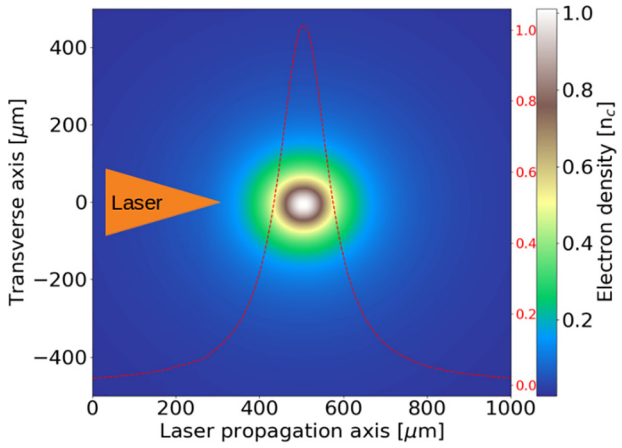

FIG. 2. Electron density distribution in the laser propagation plane. Red dashed line: electron density distribution in the direction of laser propagation. The maximum density at the center of the gas jet is $1.0n_c$.

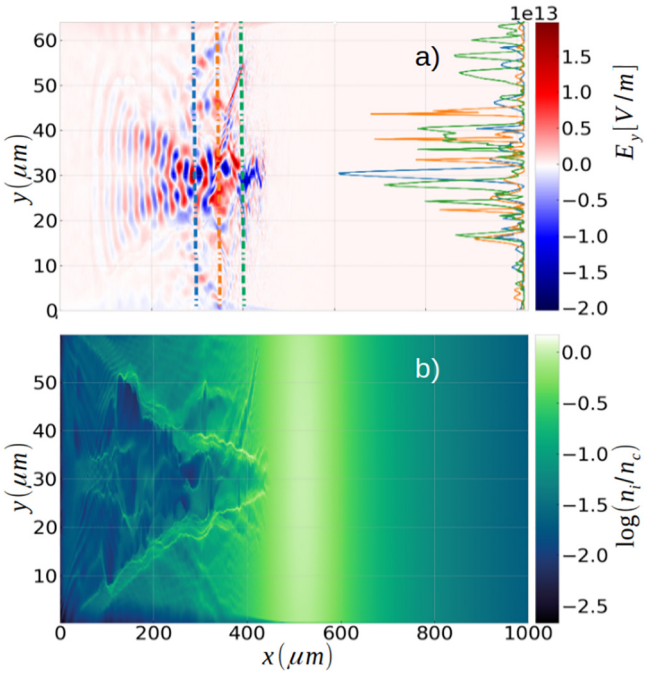

FIG. 3. (a) Left: Distribution of the laser electric field E_y in the (x, y) plane, right: $|E_y|^2$ lineouts at different positions ($x = 300$, 400, and 500 μm, proof of the laser integrity loss as a function of the propagation depth; (b) plasma density map. Laser parameters are given in the text and plasma profile is shown in Fig. 2, time is 2.4 ps.

varying from $0.01n_c$ to $0.3n_c$. The laser electric field is deteriorated during this first stage of laser propagation. The plots at the right of Fig. 3(a) in blue, orange, and green representing, respectively, the transverse distribution of the laser beam intensity as a function of the depth (at $x = 300$, 400, 500 μm) show that the laser intensity presents multiple hot spots. The radial component of the laser-driven ponderomotive force expels electrons and ions out of the central region, thus creating a density depression around the laser propagation axis with filaments between $x = 200$ and $x = 400$ μm as illustrated in Fig. 3(b).

The proton acceleration occurs in two steps:

(1) The ponderomotive force in the low density pedestal creates an electric field of charge separation and leads to proton acceleration to energies up to 20 MeV. Figure 4(a) shows that protons are accelerated in the interval between $x = 0$ and $x = 500$ μm in the low density part of plasma profile. The position of the first peak in Fig. 4(a) at $x = 150$ μm corresponds to the beginning of filamentation (after the laser beam has self-focused). The ponderomotive force in the filaments is mainly transverse, so the emission angles of the accelerated protons are centered around 90° [see Fig. 4(b)].

(2) After crossing the low density zone, the laser beam reaches a higher density and launches an electrostatic shock that accelerates protons in the forward direction. The shock is created by a pressure discontinuity due to density steepening by the laser radiation pressure. However, the energy of these protons does not exceed a few MeV due to the reduction of the laser intensity induced by strong filamentation and defocusing in the low density zone.

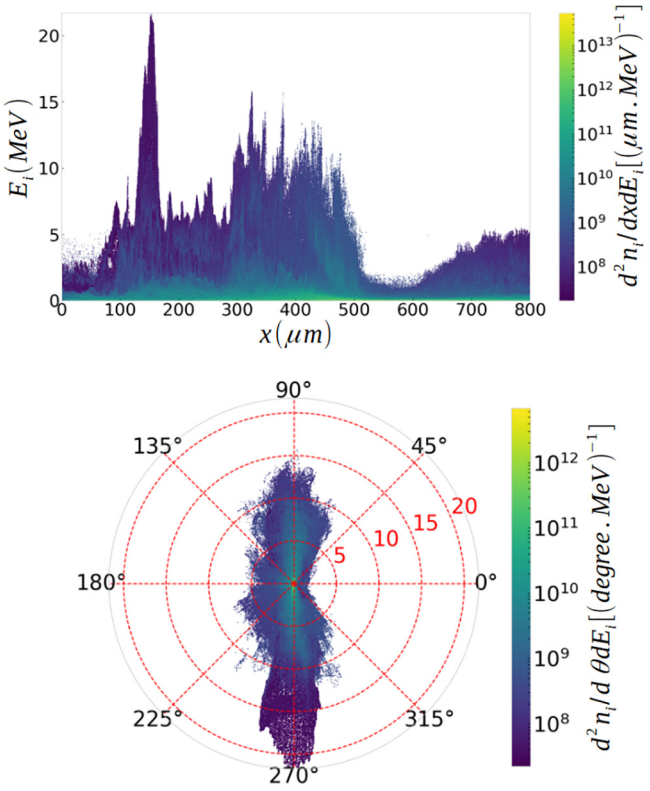

FIG. 4. (a) Proton energy E_i as a function of detection position: the most energetic protons are produced before the density peak during the laser pulse filamentation. (b) Proton energy as a function of emission angle: the most energetic protons are emitted at 90° during the laser pulse filamentation.

Figure 5 presents the proton phase diagram (p_x, x) showing the shock evolution at 6 and 19 ps. The shock is formed after the laser has left the simulation box. It propagates between 12 and 17 ps with a velocity of $0.03c$. It slows down with time in a high density ($n_e > 0.8n_c$) region of temperature $T_e \approx 50$ keV, after the peak density located at 500 μm. The corresponding Mach number of this shock is $M = 4 > 1.6$, so the ion reflection is possible.

At 6 ps, the shock front is at 500 μm. The protons located after the peak density in the gas are accelerated in a weak charge separation electric field in both directions as illustrated in Fig. 5. At 12 ps, the weak shock is propagating forward, reflecting protons in the downstream region and accelerating them to twice its velocity. After 19 ps, the symmetry between positive and negative proton momenta is broken: the protons are pushed by the shock in the laser propagation direction. There are two distinct components in the $p_x(x)$ proton diagram: the shock acceleration (red circle) and the heating (blue circle) in Fig. 5(a). This leads to two distinct components in the proton energy distribution presented in Fig. 6. This time integrated proton energy distribution in the forward direction presents a bump around 1.5 MeV corresponding to a velocity equal to twice the shock velocity. This is a confirmation of proton acceleration by the CSA mechanism,[18] whereas the left part of the spectrum corresponds to the very low energy protons not reflected efficiently by the shock but

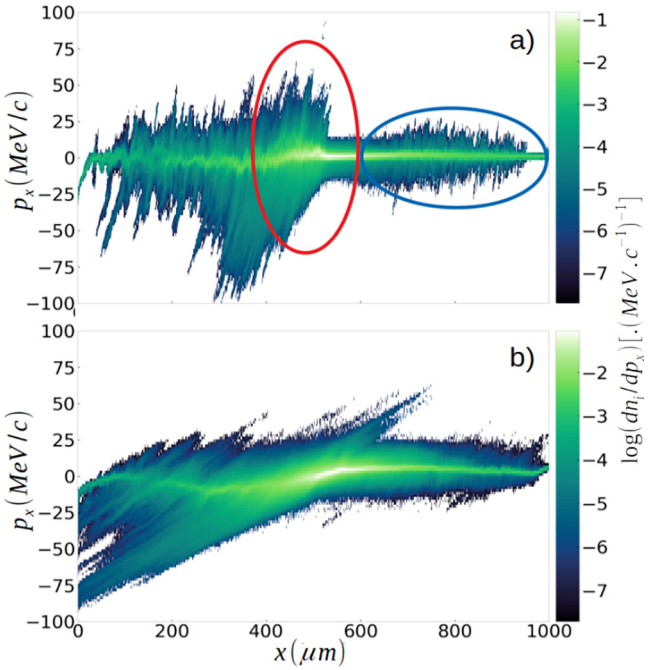

FIG. 5. Proton diagram $p_x - x$: (a) $t = 6$ ps, just after the shock formation. The red circle corresponds to the protons accelerated by CSA and the blue one to the protons accelerated by heating. (b) $t = 19$ ps during the shock propagation.

accelerated in a weak electric field of charge separation downstream of the shock. The number of accelerated protons in the forward direction by the CSA mechanism is 2.3×10^8 (the phase space of protons is transferred in 3D geometry considering a cylindrical symmetry around the x-axis on a transverse direction of the focal spot size) with energies between 0.8 and 1.8 MeV. There is a weak energy spread of the proton due to the front shock slowing down in the downstream region. These observations are in good agreement with experimental results obtained during the campaign.[23]

The main issue that prevents efficient ion acceleration in a supersonic gas jet target is therefore breaking of the laser beam in multiple filaments before reaching the density where the shock can be created. The experimental observations of low energy accelerated protons in the laser direction are explained by the laser filamentation in the gas wings. At lower laser energies (at the level of a few Joules), a laser collapse in the gas wings has also been observed to have a similar detrimental effect on CSA.[36]

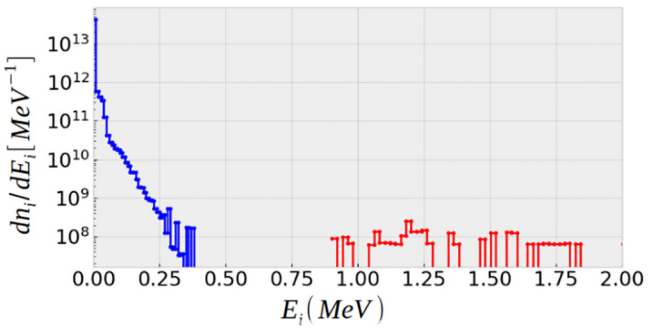

FIG. 6. Time integrated proton energy distribution in the laser beam propagation direction (angle of $\pm 0.2^\circ$). The blue part is related to the ion heating and the red one to ion acceleration by CSA.

C. Laser beam self-channeling and filamentation

Due to the finite width of the laser beam, a radial component of the ponderomotive force expels electrons out of the central region creating a density depletion. Such density decrease also increases the local refractive index and hence has a focusing effect for the pulse: this effect is referred to as "self-channeling." The position in the plasma where self-focusing starts can be estimated according to the formula proposed by Marburger[37] for the Kerr nonlinearity in optics is as follows:

$$x_f = \frac{0.367 z_R}{\sqrt{\left(\sqrt{\frac{P_{las}}{P_{cr}}} - 0.852\right)^2 - 0.0219}}. \quad (1)$$

Here, z_R is the Rayleigh length, P_{las} is the laser beam power, and P_{cr} is the critical power for self-focusing. The critical power for the relativistic self-focusing reads[38]

$$P_{cr}[GW] \simeq 17 \frac{n_c}{n_e}. \quad (2)$$

The use of the critical power for the relativistic self-focusing (2) in the Marburger formula (1) allows evaluation of the position in the plasma where self-focusing starts. For a laser power of $P_{las} \simeq 40$ TW and a Rayleigh length $z_R \simeq 1$ mm, Table I summarizes the self-focusing distance as a function of density n_e/n_c. For plasma density larger than $0.01 n_c$, this distance is much shorter than the size of the wings of the gas jet plasma. So the laser beam is strongly perturbed before reaching the central part where the shock formation may take place. In order to avoid (as much as possible) the non-linear phenomena that destroy laser beam, the length of the gas jet wings has to be reduced or their density has to be reduced by at least a factor of 10 down to the level $0.001 n_c$.

III. IMPROVING PROTON ACCELERATION BY TAILORING THE GAS DENSITY PROFILE

A. Principle of the density profile tailoring scheme

The principle of plasma tailoring proposed in Ref. 1 is illustrated in Fig. 7. A picosecond laser pulse propagates along the x-axis. The gas jet axis is placed at $x = 0$ and $y = 0$ with flow along the z-axis. One or two nanosecond (ns) laser beam(s) propagate(s) along the y-axis in the (x, y) plane at a distance b from the jet axis, typically $b \simeq 200$–300 μm in the gas jet wings. Each ns laser pulse creates a blast

TABLE I. Distance of self-focusing of a laser beam having a power 40 TW and Rayleigh length of the order of 1 mm in a homogeneous plasma of density n_e normalized to the critical density n_c.

Density ratio	Distance x_f
1	10 μm
0.1	25 μm
0.01	100 μm
0.001	500 μm

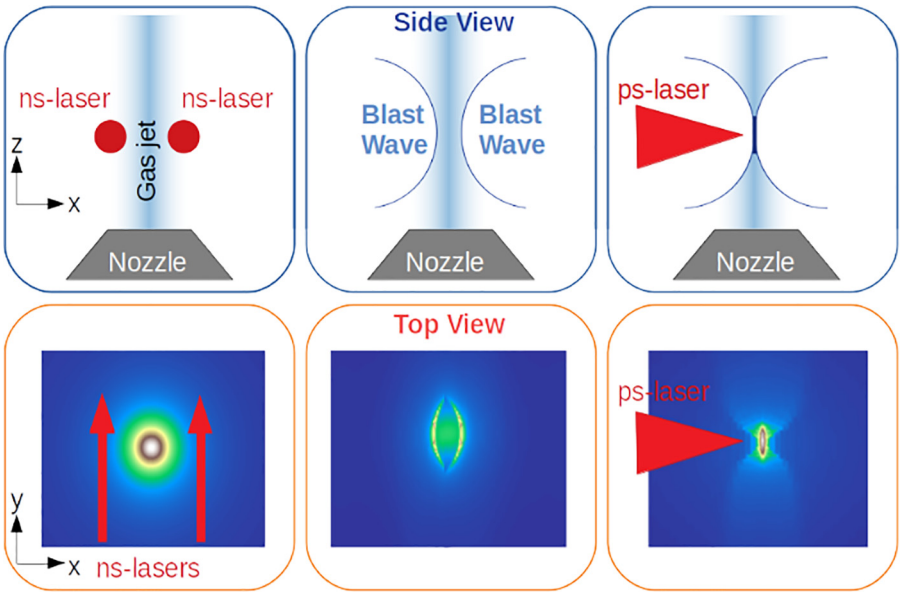

FIG. 7. Principle of plasma tailoring. Upper row: Side view (along the *y*-axis) of the gas jet exiting from the nozzle along the *z*-axis. Bottom row: Top view (along the *z*-axis). The two ns laser beams propagate parallel to the *y*-axis on both sides of the gas jet. Their absorption in the plasma creates two blast waves that collide at the center of the gas jet and produce a sharp gradient, thin, and high density plasma slab.

wave that pushes the plasma toward the center ($x = 0$) of the gas jet, increasing its density and generating a sharp density profile along the propagation axis (x) of the ps laser beam. The blast waves bending combined with their collision increases the density by more than 10 times and generates a very thin (down to a few micrometers), near to over-critical plasma layer with a high density contrast (>100), and a lifetime of a few hundred picoseconds. The plasma density profile can be modified independently at the front and rear sides of the ps-laser focal plane ($x = 0$) by adjusting the parameters of each ns-pulse (propagation distance b, focal spot size, energy and arrival times).

Hydrodynamic simulations were performed using radiation-hydrodynamics code TROLL,[27] an arbitrary Lagrangian–Eulerian mesh in two- (2D) and three- spatial dimension (3D). Since many simulations are needed to explore the parameter space (laser energy and position, gas jet density and profile) and because the characteristic density scale length along the jet axis (z in Fig. 7) is much longer than its radius, a simplified 2D geometry in Cartesian coordinates (x – y plane) has been mainly used. The simulation box is 1 × 1 mm. The gas column is at the center of the box ($x = 0, y = 0$) and corresponds to a supersonic hydrogen gas jet used in a previous experiment[23] (see Fig. 2). The hydrogen is described as a fully ionized ideal gas. However, in order to prevent an early gas jet expansion, the initial temperature is set to 300 K. Each heating-beam propagates along the y-axis at a distance $\pm\Delta x$ from the jet center, is focused at $y = 0$ in a Gaussian focal spot of 15 μm (full width at half maximum, FWHM), and has a wavelength of 1 μm and a Gaussian temporal profile of FWHM = 0.4 ns, with a maximum at t = 0.7 ns.

The plasma parameters obtained from these 2D hydrodynamics simulations (n_e, T_e, T_i, Vx, Vy the proton velocities after ns-laser pulse(s) tailoring, as function of x and y) are used for initialization of planar 2D PIC simulations with the code SMILEI.[28] The laser parameters in the simulations are the same as the simulation presented in Sec. II B. Once a proton crosses the screen diagnostics placed 5 μm before each boundary, its complete phase space is exported from the PIC simulation (position x, y, and z, momenta p_x, p_y, p_z,time t).

B. Optical tailoring at the front side

To avoid the self-focusing and filamentation of the ps laser beam, we reduce the gas density at the front part of the gas jet. To achieve this goal, a 25 J laser beam, with a Gaussian focal spot of 15 μm, a wavelength of 1 μm, and a Gaussian temporal profile of 0.4 ns FWHM is used to tailor the entrance of the gas jet. This laser beam is focused at 250 μm from the gas jet center (see TROLL simulations in Ref. 1). A set of four PIC simulations of ps laser interaction with preformed plasma were performed at four different delay times with respect to the ns-laser pulse. The plasma density profiles between 0.1 and 1.2 ns are shown in Fig. 8. At 0.1 ns, the density profile of the gas jet is the same as the one used in Sec. II B. (see Fig. 2) with a maximum density of $1.0n_c$ at the center of the plasma profile.

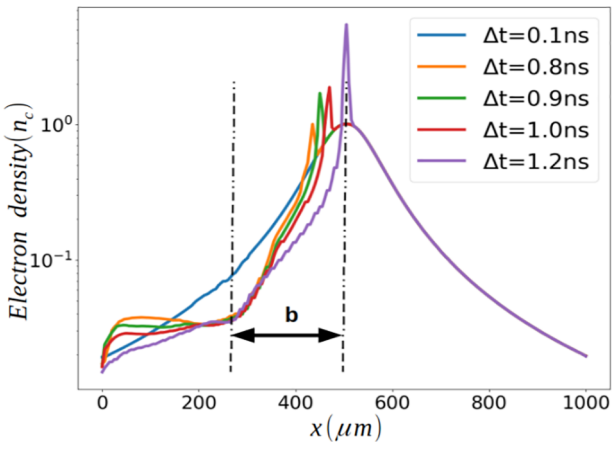

FIG. 8. Time evolution of the plasma density profile between 0.1 and 1.2 ns after ns-laser absorption along the laser propagation axis. In this case, the propagation distance between ns-laser focus and peak density is set to 250 μm. The maximum density varies from $1.0n_c$ at 0.1 ns to $5.3n_c$ at 1.2 ns.

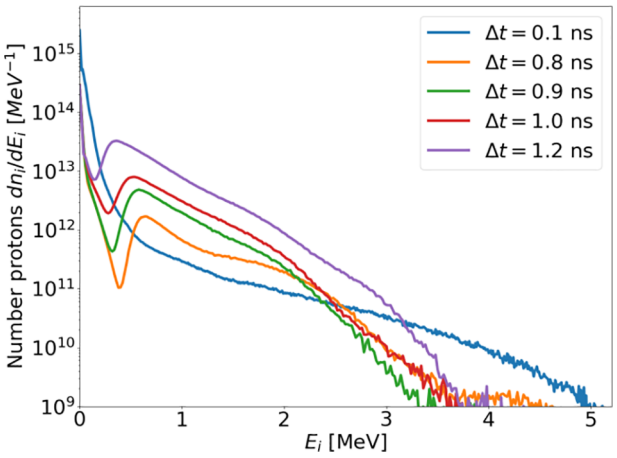

FIG. 9. Energy distribution of accelerated protons in the forward direction as a function of the density profile presented in Fig. 8 with initial density of 1.0 n_c and plasma tailoring at the front side.

The energy deposition of the tailoring laser induces blast waves propagating in opposite directions and a local density depletion as shown in Fig. 8 at $x = 250\ \mu$m. The blast wave propagating to the gas jet center increases the maximum density from n_c to $5.3n_c$ in this region. Nevertheless, the density depletion in the wings is not as large as required for reducing the non-linear processes. At a distance of 250 μm from the jet axis, the density decreases only by a factor of two and not by a factor of 10 as required. Thus, the density in the gas wings is not enough reduced, and the laser beam integrity is not preserved during the laser propagation. Compared to the case without tailoring, the self-focusing distance is longer (the filamentation starts about 80 μm further) due to the local density depletion. However, the proton acceleration is not enhanced in the direction of the laser propagation.

The proton energy distributions in the forward direction obtained in these simulations are presented in Fig. 9. Using a gas jet with initial density of n_c modified by a ns-laser at the front side increases the number of accelerated protons by a factor 7.5 (see Table II) at the maximum compression delay time of 1.2 ns. This is explained by a shock created earlier in the density ramp rise and a larger number of protons that crossed the shock front in the upstream region. Indeed, depending on the delay time, as presented in Fig. 8, the shock crossed a higher proton density for the larger delay times. The proton cutoff energy is a bit lower with gas tailoring because the temperature at the rear side of the gas jet is lower, leading to a weaker shock.

TABLE II. Number of accelerated protons in the forward direction and cutoff energy as a function of the maximum density in the shock front.

Delay time (ns)	$n_{e,\max}/n_c$	Protons $E_i > 1$ MeV	Cutoff energy
0.1	1.00	2.4×10^{13}	5.0 MeV
0.8	1.02	2.8×10^{13}	4.5 MeV
0.9	1.71	4.5×10^{13}	3.5 MeV
1.0	1.90	7.2×10^{13}	3.8 MeV
1.2	5.30	1.8×10^{14}	3.7 MeV

The proton acceleration can be still improved: in order to completely suppress the filamentation process and enhance the proton acceleration in the forward direction, the density in the gas wings has to be decreased down to a level of $0.001n_c$ as estimated in Sec. II C., assuming a maximum density of $0.1n_c$ before the tailoring process.

C. Creation of a very low density pedestal at the front side

Other sets of 2D planar PIC simulations were performed using the same gas target but with an initial density 0.10 n_c: one without optical tailoring, another with ns-laser tailoring at the entrance of the gas jet, and the third one with initial density 0.20 n_c with ns-laser tailoring. As shown in Fig. 10, the electron density peaks in these simulations are, respectively, 0.10 n_c, 0.41 n_c, and 1.08 n_c.

1. Case without tailoring–initial density 0.10 n_c

The filamentation is suppressed and the laser beam integrity is preserved during its propagation in the low density pedestal as shown in Fig. 11. The self-focusing of the laser occurs from $x = 350\ \mu$m, inducing an intensity increase by a factor 2.3 between $x = 350$ and $x = 400\ \mu$m as shown in Fig. 11(a).

The maximum density at the center of the gas jet is $0.1n_c$, so the ps-laser with $a_0 \approx 6$ can cross entirely the gas, producing a strong bulk heating. The protons are expelled from the maximum density region by the laser ponderomotive force in the transverse direction as shown in Fig. 12(a) on the laser path. In the very low density region behind the peak density, the laser heats electrons (up to 800 keV) and induces wave breaking that evolves in several shocks as shown in Fig. 12(b) after $x = 650\ \mu$m. These shocks are weak and are created in a region where many protons are pushed by the laser ponderomotive force up to kinetic energies between 2 and 10 MeV, so the efficiency of the proton acceleration can still be improved.

The use of a lower initial density strongly reduces the laser beam energy loss: the laser beam reaches the higher density region of the plasma without a notable energy loss. Consequently, the proton acceleration is more efficient than in the case of a gas jet target with a density of $1.0n_c$: as illustrated in Fig. 13(a), the protons are mainly

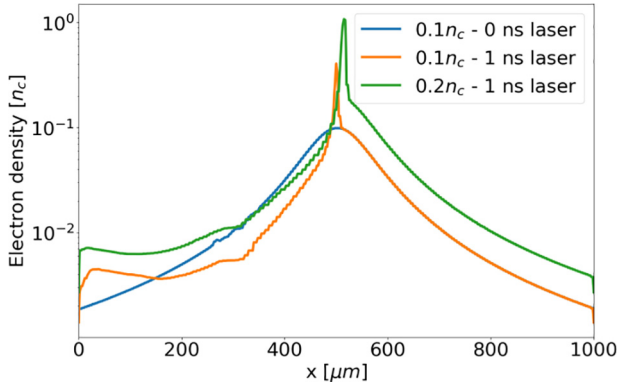

FIG. 10. Electron density profiles in the gas jet with the initial density is divided by 10 (orange) and by 5 (green) (compared to the profiles shown in Fig. 8) with ns-laser tailoring at the entrance of the gas jet and without tailoring (blue).

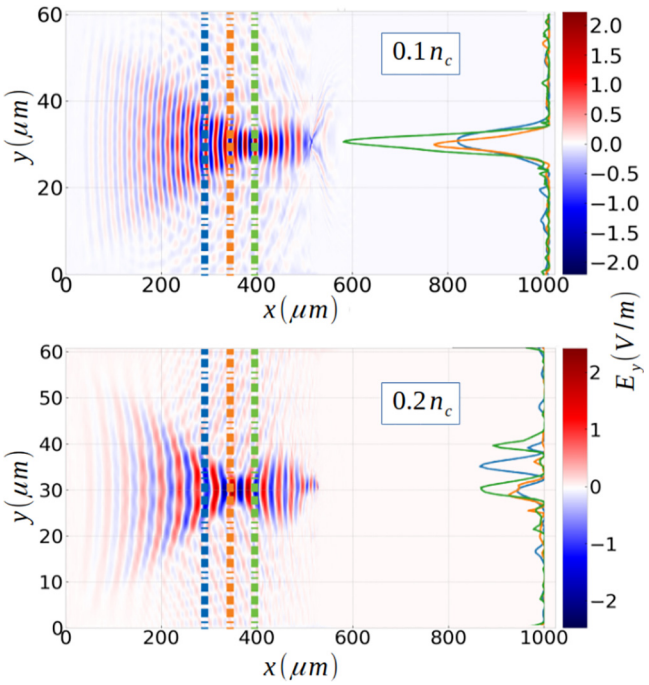

FIG. 11. Distribution of the laser electric field E_y in the (x, y) plane (left)—$|E_y|^2$ line-outs at different positions ($x = 300$, 400, 500 μm), showing the laser integrity loss in the gas jet density ramp (right)—the initial density is $0.10n_c$ (top) and $0.20n_c$ (bottom) and is modified by one ns-laser pulse, time is 2.4 ps.

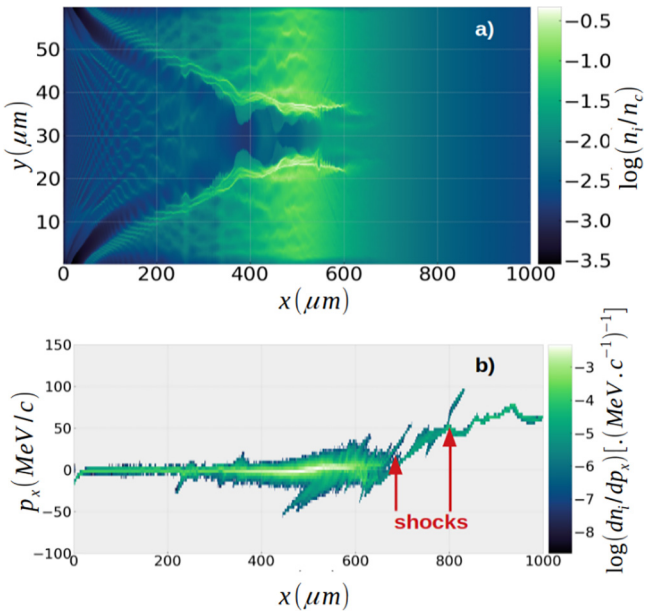

FIG. 12. (a) Spatial distribution of proton density at 3.5 ps just after the laser has passed through the high density region. (b) Proton phase space diagram at 7 ps with two shock structures. Case without tailoring—initial density 0.1 n_c.

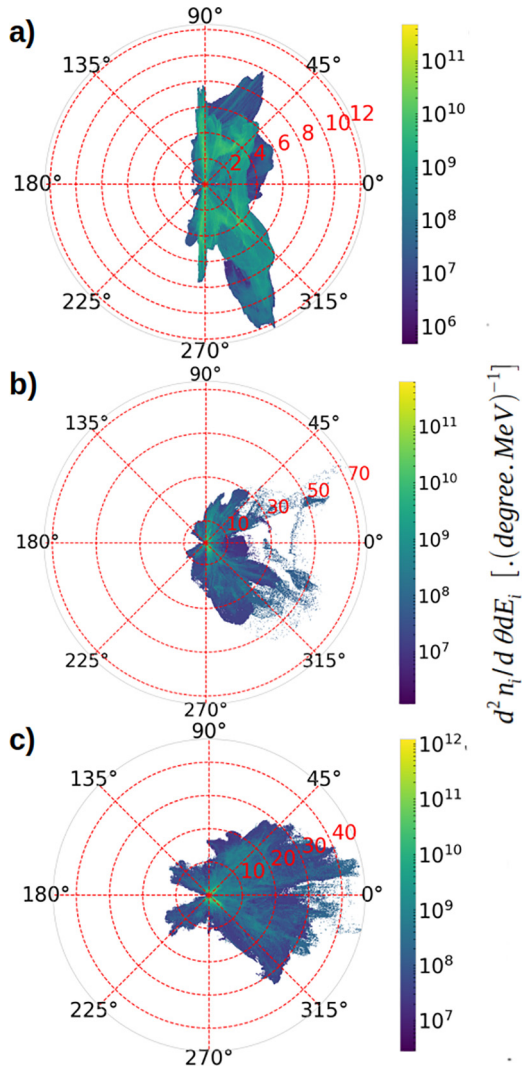

FIG. 13. Angular proton energy distributions: (a) case with no tailoring density profile; (b) case with front side tailoring and an initial density of $0.1n_c$; and (c) case with front side tailoring and an initial density of $0.2n_c$.

accelerated in the tranverse direction with lower energies (up to 12 MeV), whereas in the forward direction, the proton energy reaches 5 MeV. However, the proton acceleration efficiency is still low: the maximum density is $0.1n_c$, so the gas target remains transparent for the ps laser beam, the transmission coefficient of the plasma is too high (about 70%) and the conversion efficiency is low: only 11% of the laser energy is transferred to the plasma electrons and 2% to protons. The high density region has to be denser to allow a better laser energy conversion.

2. Case of laser plasma tailoring—initial density 0.10 n_c

As presented in Fig. 10, the use of one ns laser at the entrance of the gas jet allows us to create a narrower plasma region with a peak density up to $0.41n_c$ at the center of the gas jet, suitable for electrostatic

shock formation and efficient proton acceleration in the forward direction. The low density in the gas wing at the entrance of the gas jet allows us to keep the laser integrity, as illustrated in Fig. 11: with an initial density of 0.1 n_c, with or without tailoring, the filamentation is suppressed. Comparing panels a and b in Fig. 13 and presenting the angular proton energy distributions, the acceleration process is significantly improved with the tailoring at the entrance of the gas jet: in the forward direction, the protons reach energies close to 70 MeV within emission angles less than 30°. At 0°, the proton energy is about 20 MeV with some bunches of protons that reach 30 and 40 MeV. The increase in the density at the center of the gas jet allows for a better laser absorption and thus improves the conversion efficiency of the laser even if the plasma remains transparent: the laser absorption is 35% (27% in electrons and 8% in protons).

The acceleration proceeds in two stages:

(1) The first acceleration stage is governed by a TNSA-like mechanism and takes place near the high density layer. At 2.1 ps, the laser pulse penetrates through the high density region, and its ponderomotive force pushes a part of the electrons forward and forms a sheath at the target rear surface that presents a sharp density gradient. The accelerated fast electrons reach energies up to 100 MeV. The current of these hot electrons is so important that a magnetic dipole with a maximum magnetic field intensity of about 2×10^4 T at the time 3 ps is formed at about $x = 580$ μm at the rear side of the density peak. As observed in a previous experiment[39] and explained numerically,[40] this magnetic field induces electric fields due to its variation over time associated with the fast electronic current, providing a contribution to the accelerating TNSA-like sheath field. The quasistatic magnetic field is likely to enhance the charge separation to extend the lifetime of the sheath field and centrally focuses electrons, generating a collimating radial electric field for ions. As illustrated in Fig. 14(a), at 2.6 ps, the sheath electric field with amplitude of 0.6 TV/m induces a TNSA-like ion acceleration. Then, the laser reaches the sharp part of the density profile, keeping on accelerating electrons up to a hundred MeV and breaking the steep density profile at the rear side of the plasma. The heated electrons propagate through the rear side of the plasma, driving a return current that pulls the background electrons to the laser region where they are accelerated. The early build-up of the return current with the quick recirculation of the heated electrons due to the space-charge fields at the rear side of the plasma tends to uniformize the temperature profile after the high density region. The electron temperature reaches 3 MeV during the shock propagation in the low density ramp. The TNSA-like field accelerates a bunch of protons to 70 MeV. The rear side of the gas curved by the laser ponderomotive force, together with the two magnetic lobes created close to the sharp density gradient, accelerates protons off the laser axis with an angle of 30° [see Fig. 13(b)].

(2) The second acceleration stage is governed by a shock-like mechanism: a large fraction of proton population is thus accelerated by the charge separation layer due to the hot electrons driven by the laser. These accelerated protons evolve into acoustic wave breaking in the region after the peak density. The electrostatic shock formed at about 4 ps, after the expulsion of proton bunch accelerated by TNSA-like mechanism, propagates downstream and reflects protons. In Fig. 14(c), at 8 ps, three shocks structures are present with their corresponding electric fields, and give rise to three energy ranges in the proton energy distribution in Fig. 13(b). The first shock (shock 1) in Fig. 14(c)

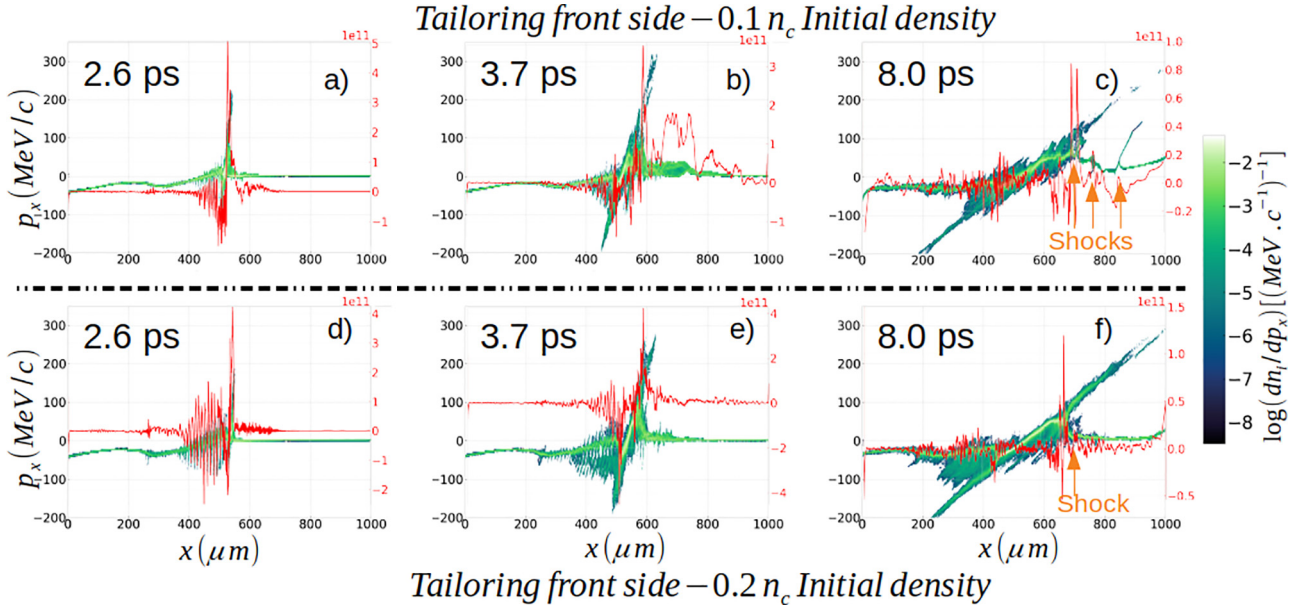

FIG. 14. Proton $p_x(x)$ diagram and superposed electric field E_x averaged on the whole y-axis in red for tailoring at 0.1 n_c density (top row) and for the tailoring at 0.2 n_c density (bottom row). Panels correspond to the time moments of 2.6, 3.7, and 8.0 ps.

has a velocity of 0.14c between 4.2 and 8 ps and then slows down to 0.12c at 20 ps, corresponding to a proton energy range between 27 and 37 MeV. These protons are reflected from the shock front since it is characterized by a Mach number $M = 2 > 1.6$, which is able to reflect protons. The secondary shocks, created later, at 5.5 and 9.5 ps in a high temperature and low density region ($x > 650$ μm), present maximum velocities of 0.09c and 0.04c, corresponding, respectively, to proton energies of 16 and 3 MeV. These three shocks contribute to the proton angular spectrum distribution in Fig. 13(b), in the forward direction, in a quite narrow emission angle of 5°. The formation of several shocks is due to the long pulse duration that produces several pressure discontinuities in a hot plasma.

3. Case of laser plasma tailoring–initial density 0.20 n_c

In the case of laser tailoring of a plasma with the maximum density of 0.20 n_c, the main laser pulse loses some energy during its propagation in the gas jet wing as explained in Sec. II C due to a higher density in the entrance wing of the gas jet than in the case of a maximum density of 0.10 n_c. Thus, when the laser reaches the high density region, as illustrated in Fig. 11, the laser intensity is four times smaller than in the case with the density 0.10n_c considered above. Comparing shocks structures between these two cases in Fig. 14, the latter case corresponds to a smaller shock velocity: due to the laser energy loss in the plasma pedestal, the electron heating is less efficient in the dense layer. Moreover, the density in the target is 2 times higher, so the shock dissipates more energy in the plasma during its propagation at the rear side of the gas jet. Consequently, as presented in Fig. 13c, and compared with Fig. 13(b) for the case at 0.10 n_c, the protons are still accelerated in the forward direction but the proton energy distribution is broader due to a higher density after the peak density where the shocks slows down, spreading the proton energy distribution. Also the proton cutoff energy is lower (40 MeV).

Figure 15(c) presents the corresponding proton energy distribution integrated in time at different angles: $\theta = 0°, 22°, 45°$, and 90° obtained by integrating the distribution $d^2n_i/d\theta dE_i$ in a cone of ±5°. The use of laser plasma tailoring improves the proton acceleration in terms of direction, energy, and number:

- In the forward direction, the proton cutoff energy increases from a few MeV without tailoring to several tens of MeV with bunches of protons up to 40 MeV at 0°. The decrease of the proton energy cutoff when the initial density is doubled is due to the laser energy loss in the wing before the shock creation.
- The angular distribution of accelerated protons is better aligned in the forward direction in a tailored plasma: the number of accelerated protons at 90° is reduced by a factor of 5, while the number of protons accelerated at 0° is increased by a factor of 2.
- The angular distribution of accelerated protons is narrower in the tailored plasma. It is limited to the range of angles between 0° and 30°.

The front-side laser tailoring of the plasma density profile before the main ps-laser shot improves the proton acceleration in terms of energy, number and directionality. The use of plasma with density 0.10 n_c gives the best results in terms of proton maximum energy since the laser pulse is not perturbed in the pedestal, and it creates a strong shock

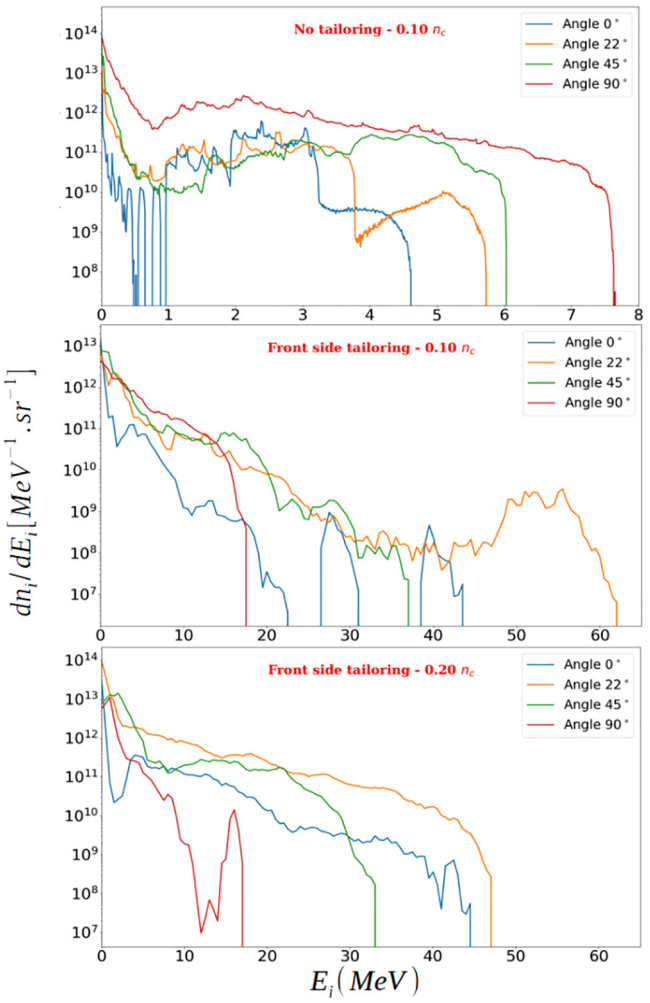

FIG. 15. Proton energy distributions integrated in time at angles: $\theta = 0°, 22°, 45°$, and 90° obtained by integrating the distribution $d^2n_i/d\theta dE_i$ in a cone of ±5°: (a) case without laser tailoring, (b) case with front laser tailoring and an initial density 0.10 n_c, and (c) case with front laser tailoring and an initial density 0.20 n_c.

in the compressed plasma layer with less dissipation in the region of a low plasma density. For the case with density of 0.20 n_c, the shock propagates with a lower velocity (the laser pulse has lost more energy in the higher density entrance wing) so the proton cutoff energy is lower but the number of accelerated protons in the laser direction is twice larger than in the case of a density twice lower. Thus, a quasi-monoenergetic distribution of accelerated protons is obtained with the lowest density, with energies around 30 and 40 MeV, energy spread of about 16%, and number close to 5×10^9 protons per steradian.

The tailoring at the front side of the gas jet target strongly improves the proton acceleration in a gas target, but using only one ns-laser pulse at the front side presents a limitation of a peak density in the compressed layer, which is not high enough to approach the condition[18] $n_e \cong a_0 n_c$ for a strong shock formation. Adding a second ns laser at the rear side allows us to create a higher and narrower density layer at the center of the gas jet.

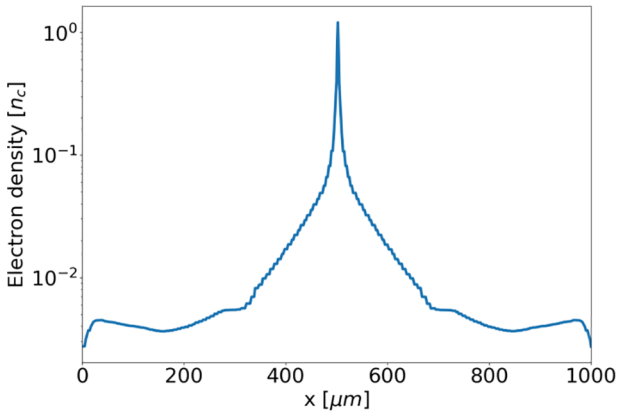

FIG. 16. Density profile of the gas jet along the main laser propagation axis shaped with two ns-lasers. Initial density in the gas jet is $0.10n_c$. After tailoring both front and rear sides of the plasma, the maximum density at the center of the gas jet is $1.4n_c$ and the width of the central peak is about 5 μm.

IV. OPTICAL TAILORING OF THE FRONT AND REAR SIDES OF THE GAS JET

A. Creation of a narrow high density peak by tailoring both the rear and front sides of the gas jet

Tailoring the entrance of the gas jet allows us to work with a low gas density and suppresses non-linear processes in the gas jet pedestal. However, the maximum density only reaches $0.41n_c$ over a distance of several micrometers and the plasma remains transparent for the ps-laser beam. The use of a second ns-laser beam at the rear side induces a second hydrodynamic counterpropagating shock, and if the ns-laser beams are synchronized, both shocks collide at the gas center. Figure 16 presents the density profile at a high compression at 1.4 ns after the interaction with the two ns-laser beams, allowing us to reach a higher peak density of $1.4n_c$ and a thin layer of FWHM of about 5 μm.

The preservation of the laser beam quality and the increase in maximum density in the compressed layer allow us to accelerate protons up to 60 MeV. As illustrated in Fig. 17, the proton beam is well collimated: the protons are mainly accelerated between 0° and 45°.

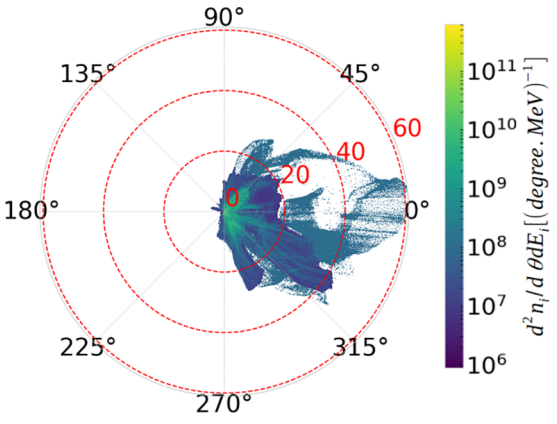

FIG. 17. Angular proton energy distribution in the case of two ns-laser tailoring with initial density $n_0 = 0.1n_c$ after 1.4 ns.

Compared to the case of plasma tailoring with one ns-laser [see Fig. 13(b)], some bunches of accelerated protons are present in the forward direction at 0° but with a larger energy spread. The proton cutoff energy is slightly lower and at high energies (> 60 MeV); acceleration is more efficient in the forward direction.

Figure 18 shows time evolution of the acceleration process. The laser energy is transferred to electrons with an efficiency of 23%, and then 9% of this energy is transferred to protons. The laser transmission coefficient is about 40% because the plasma is transparent for the laser pulse. The peak density value of $1.4n_c$ is smaller than the relativistic critical density for the laser pulse ($\gamma n_c \approx \sqrt{1+a_0/2}n_c = 4.4n_c$). The acceleration process proceeds in two steps with a TNSA-like stage followed by shock-like acceleration.

At 2.6 ps, the electrostatic field reaches the value of 1 TV/m but 100 fs after, as illustrated in Fig. 18(a), and a second spike of electrostatic field with amplitude of 0.7 TV/m is created by laser-accelerated hot electrons. These two spikes of electric field combine and at 3.7 ps [see Fig. 18(b)] create one strong shock and additional multiple weaker shock structures. This process can be considered as wave breaking [see Fig. 18(c)]. The most remarkable difference between the phase spaces in Figs. 14 and 18 is that the upstream protons before shock reflection are not at rest at earlier times (see the central plot in both figures), but have a small uniform momentum. This is a consequence of a steeper density profile at the rear side of plasma, which leads to the development of a higher TNSA-like field. Moreover, the shock propagates through a plasma with a high electron temperature of 8 MeV and can accelerate protons to higher energies since the shock velocity is directly linked to the electron temperature.

Figure 19 presents the proton energy distribution integrated in time at angles: $\theta = 0°, 22°, 45°$, and 90° obtained by integrating the distribution $d^2n_i/d\theta dE_i$ in a cone of ±5°. Compared to the front ns-beam tailoring, the use of two ns-laser beams improves proton acceleration in the forward direction. At 0°, a clear signature of CSA is present with a bump of protons with energies centered on 50 MeV with energy spread (≈ 40%) and with a particle number of 2×10^{10} per steradian. A similar structure (but smaller in terms of number and energy) is present at 22°.

V. OPTIMIZATION OF THE SHOCK ACCELERATION SCHEME

Plasma tailoring with two ns-laser beams leads to significant improvement of proton acceleration in terms of maximum energy, angular distribution, and number. Another advantage using two ns-lasers is the presence of the quasi-monoenergetic features in the energy spectrum in the forward direction. The acceleration process can be further improved by optimizing the density, thickness of the gas jet, or the density gradient of the wings encountered by the main ps-laser beam.

A. Effect of the density peak maximum value

The maximum value of the density profile is a key parameter for efficient shock acceleration. It defines the time of shock formation and the shock velocity. If the main pulse is launched at 1.45 ns, that is, just 50 ps later than in the previous case, the maximum plasma density reaches a value of $2.1n_c$. The only difference with the density profile presented in Fig. 16 is the maximum density value. The protons are accelerated to higher energies with a cutoff energy of 70 MeV [see Fig. 20(a)] in the forward direction. Consequently, a higher maximum

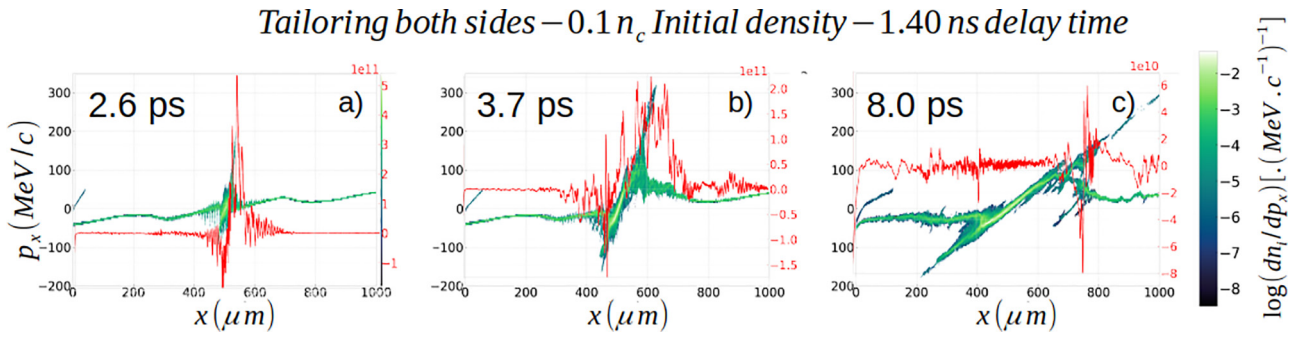

FIG. 18. At times 2.6, 3.7, and 8 ps, proton $p_x(x)$ diagram and superposed electric field E_x averaged on all y-axis in red.

density value in the compressed layer improves the proton acceleration. Figure 20(b) presents the proton energy distribution with a clear signature of CSA with a bump of protons around 55 MeV with an energy spread less than 14% and with a number of particles of 10^{10} per steradian.

A variation of the maximum density from $0.1n_c$ to $7n_c$ has been tested for the density profile obtained with two ns-laser plasma tailoring, using the density profile presented in Fig. 16 and applying a given multiplicative factor (the whole density profile was multiplied by this factor, so the density gas wings was also multiplied by the same factor). Figure 21 shows dependence of the maximum proton energy on the maximum plasma density. There is an optimal maximum density in the range between $0.8n_c$ and $3n_c$ corresponding to a proton cutoff energy above 40 MeV. The use of a gas with an initial density 0.1 n_c combined with the two ns-lasers tailoring allows us to obtain a compressed plasma layer with density around $2n_c$, leading to the most efficient proton acceleration. For the maximum plasma density greater than $3n_c$, CSA becomes less efficient because the shock is created earlier in the plasma and is weaker.

B. Effect of the width of compressed layer

In order to increase the number of accelerated protons in the shock front, the thickness of the compressed layer was increased, as illustrated in Fig. 22, from 5 to 20 μm. Such a profile of compressed plasma layer can be obtained with longer time delays between the ns and ps pulses (see Ref. 1).

When the thickness of the compressed layer increases, the acceleration process is deteriorated. With a plateau of 5 μm (orange curve), as presented in Fig. 22(a), the proton energy is reduced to 40 MeV, and no spike signature is observed in the proton energy distribution [see Fig. 22(b)]. The shock is formed earlier in the plateau.

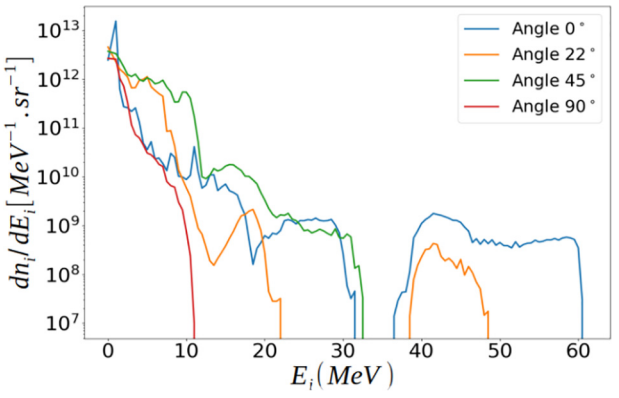

FIG. 19. Proton energy distribution integrated in time at different angles: $\theta = 0°, 22°, 45°$, and $90°$ obtained by integrating the distribution $d^2n_i/d\theta dE_i$ in a cone of $\pm 5°$ in the two ns-beams tailoring case.

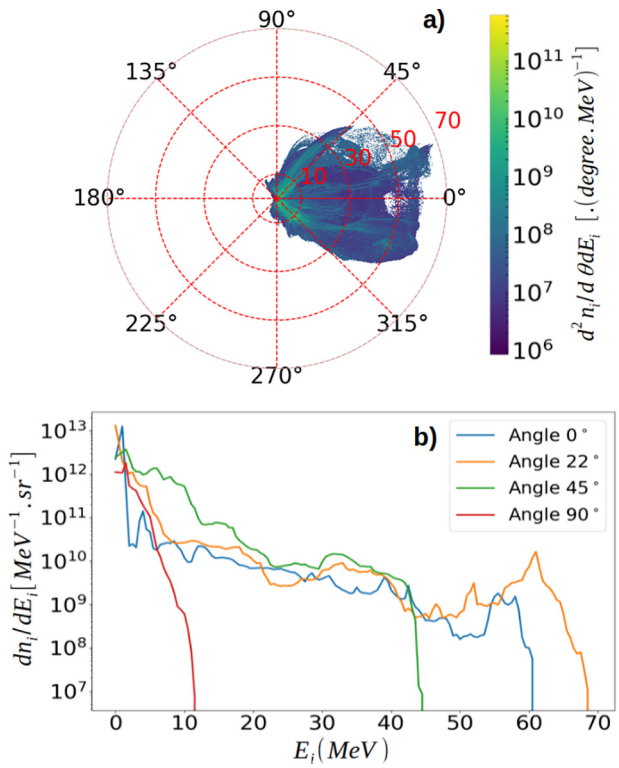

FIG. 20. (a) Proton energy as a function of emission angle in the case of two ns-laser tailoring with initial density $n_0 = n_c/10$ after 1.45 ns. (b) Proton energy distribution integrated in time at different angles: $\theta = 0°, 22°, 45°$, and $90°$ obtained by integrating the distribution $d^2N_p/d\theta dE_{kin}$ in a cone of $\pm 5°$ in the two ns-beams tailoring case with initial density $n_0 = n_c/10$ after 1.45 ns.

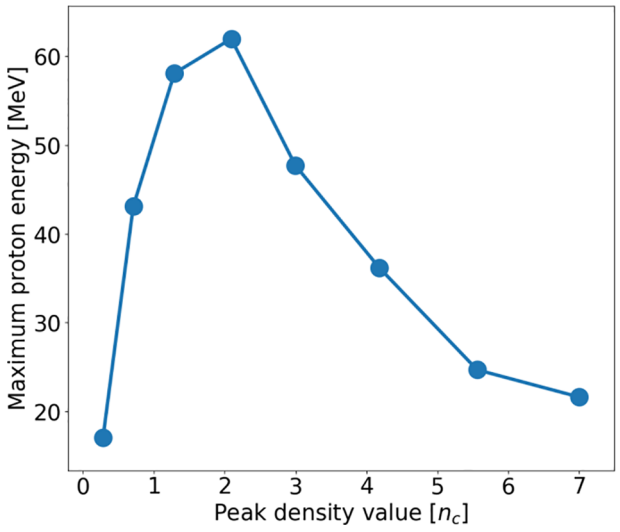

FIG. 21. Maximum energy of accelerated protons as a function of maximum density value of the compressed plasma layer at the center of the gas jet.

The spectrum at every angle is broadened. As the shock propagates through a larger plateau (not shown), it continuously slows down leading to proton acceleration to smaller energies. Thus, increasing the plateau width is not improving the proton acceleration, neither in terms of maximum energy nor number. An alternative solution for the creation of a step-like shape for the compressed layer is considered in Sec. V C.

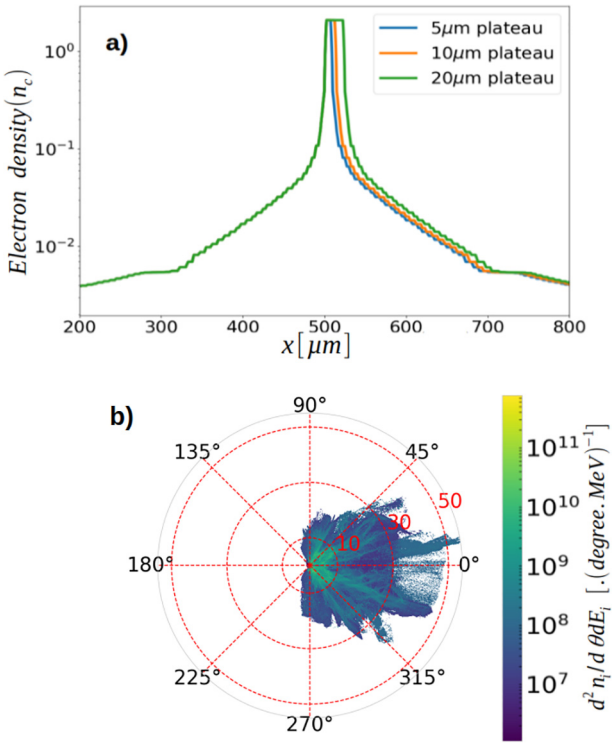

FIG. 22. (a) Density profiles used for the different PIC simulations. Maximum density is 2 n_c. (b) Angular proton energy distributions computed for the case of the 5 μm plateau.

C. Effect of the shape of compressed layer

Figure 23 presents the density profiles obtained from hydrodynamic simulations at the maximum compression at 1.4 and 1.5 ns in the case of two ns-laser pulses. The FWHM of the density spike is 2.1 μm at 1.4 ns and 4.5 μm at 1.5 ns. This profile broadening is associated with a decrease in the maximum density by a factor of 2.

The acceleration process is significantly improved in terms of proton energy: as illustrated in Fig. 24, in the forward direction, the protons reach energies close to 70–80 MeV. The angular distribution is narrowed to 10° with respect to the laser propagation axis.

The laser energy transfer to electrons is 28% and 11% of this energy is transferred to protons. The laser transmission coefficient is 40%.

The acceleration process is a combination of TNSA and CSA. As illustrated in Fig. 25 at 2.6 ps, the laser creates a shock at the beginning of the compressed layer, which is manifested by the ambipolar longitudinal field of 30 GV/m just before $x = 500\ \mu$m. At the same time, a strong TNSA field is created at the rear side of the compressed density layer. The shock catches up the TNSA field and creates a stronger acceleration field at $x = 600\ \mu$m and $t = 3.7$ ps. The two combined shocks reflect ions that are pre-accelerated in the TNSA electric field. The proton energy distribution in the forward direction has a TNSA-like exponential shape. Figure 24(b) presents the proton energy distribution integrated in time at angles: $\theta = 0°, 22°, 45°$, and 90° obtained by integrating the distribution $d^2n_i/d\theta dE_i$ in a cone of $\pm 5°$. Compared to the two beams tailoring at 1.4 ns, broadening the density layer improves the proton acceleration in the forward direction. The cutoff energy is 80 MeV at 0° and the number of accelerated protons with energies higher than 60 MeV is 3×10^9 per steradian.

VI. DISCUSSION

This new scheme of tailoring both sides of a supersonic gas target allows us to reach proton energies never achieved with realistic plasma

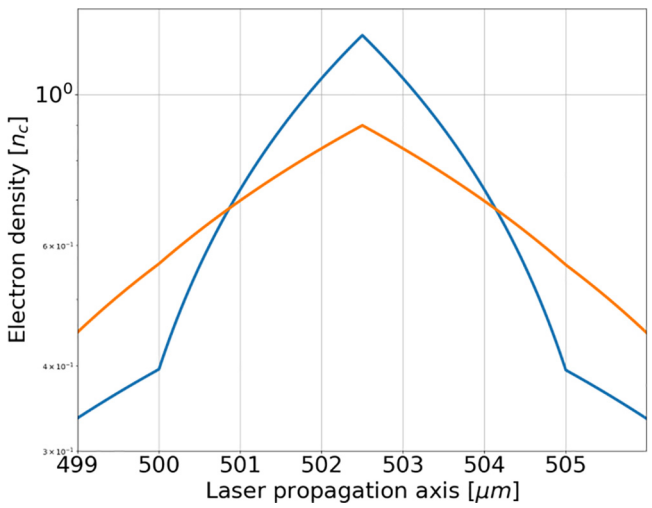

FIG. 23. Zoom of density peak region in the case of two ns-beams, 1.4 ns (blue curve) and 1.5 ns (orange curve), after the ns-lasers are shot.

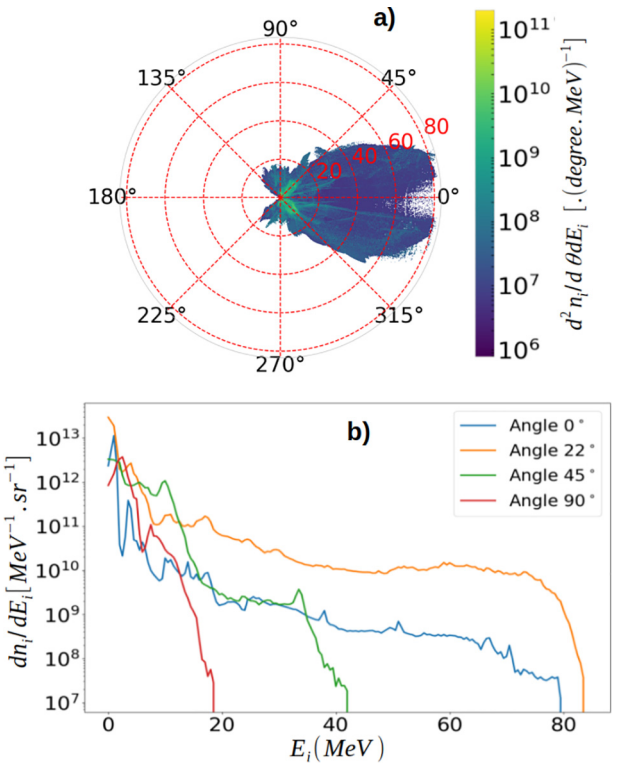

FIG. 24. (a) Proton energy as a function of emission angle in the case of two ns-laser tailoring with initial density $n_0 = n_c/10$ at 1.5 ns after the ns-laser are shot. (b) Proton energy distribution integrated in time at angles: $\theta = 0^\circ, 22^\circ, 45^\circ$, and 90° obtained by integrating the distribution $d^2n_i/d\theta dE_i$ in a cone of $\pm 5^\circ$ in the two ns-beams tailoring case at 1.5 ns.

density profiles in this regime. For applications, proton acceleration in the forward direction is the most interesting geometry. Figure 26 summarizes the best proton energy distribution at 0° obtained in this work, i.e., with the two ns laser tailoring at different delay times. The proton energy cutoff varies from 60 to 80 MeV. Shock structures are present in the proton energy distributions with a variable width. At a delay of 1.40 ns, a bunch of accelerated protons with energies centered at 50 MeV with energy spread (≈40%) and with a number of 2×10^{10} per steradian are obtained. At a delay of 1.45 ns, the proton

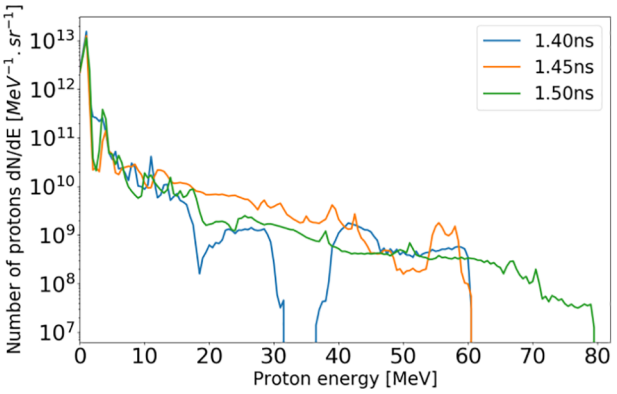

FIG. 26. Comparison of the proton energy distribution integrated in time at $\theta = 0^\circ$ obtained by integrating the distribution $dn_i/d\theta dE_i$ in a cone of $\pm 5^\circ$ in the two-sides tailoring case depending on delay time.

energy distribution is broadened with a maximum shifted to 55 MeV and with a number of 10^{10} protons per steradian. At a delay of 1.50 ns, the proton energy distribution takes an exponential-like shape and with a number of accelerated protons with energies greater than 60 MeV of about 3×10^9 per steradian.

The specific interest of this scheme consists in the fact that the proton energy distribution can be adjusted depending on the application. For parameters such as the number of ns-beams, the delay time and the position of the ns-beam allow us to shape the gas density profile.

VII. CONCLUSION

We present the analysis of proton acceleration in the interaction of an intense ps laser pulse with a gas jet plasma by using 2D PIC simulations. A typical gas jet has a few millimeters width, which strongly deteriorates the angular distribution and energy spectrum of accelerated protons. The use of one or two additional ns laser pulses allows us to shape independently the density profile at the front and rear sides of the gas jet. The ns laser beams heat and expel the plasma and create blast waves that compress the gas density at the center. By choosing an appropriate delay between the ns and ps laser pulses, one can optimize the conditions of proton acceleration, their energy distribution, and energy cutoff.

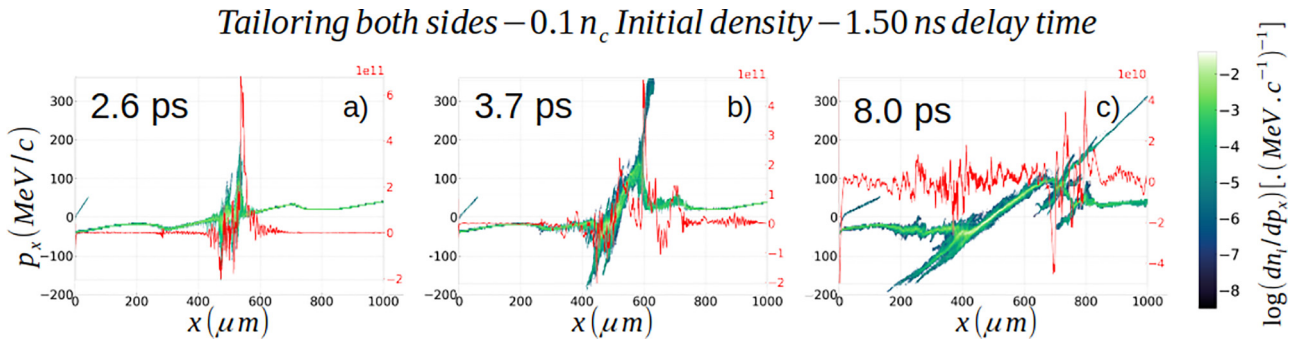

FIG. 25. Proton $p_x(x)$ diagram and superposed electric field E_x averaged on all y-axis in red for time moments of 2.6, 3.7, and 8.0 ps.

A very low density pedestal followed by a narrow compressed region created by the blast waves is favorable for the creation of a strong shock. The shape of the rear side density profile controls the competition between the TNSA and CSA processes. A combination of these two processes allows us to accelerate protons to high energies. Thus, plasma tailoring with ns pulses allows us to approach the conditions for an efficient CSA formulated in Sec. I and illustrated in Fig. 1.

- In order to preserve the laser pulse integrity, the better initial density of the gas jet before the tailoring process is $0.1n_c$ at the center of the gas jet. Thus, the density in the gas wing entrance is low enough to allow the laser to keep its integrity. The two blast waves created by the optical tailoring allow us to obtain a high density region at the center of the plasma while guaranteeing a low density pedestal that allows us to keep the laser integrity.
- In order to create a strong shock, the peak plasma density must be on the order of the relativistic critical density[18] $n_e \cong a_0 n_c$. For the initial maximum density of $0.1n_c$, one has to create a plasma compression by a factor of 20 assuming the dimensionless amplitude of the main laser pulse a_0 is on the order of unity. Such a compression on the axis of the gas jet by using two ns laser beams that produce two converging blast waves creates a thin, high density plasma layer at the moment of the collision. The optimum density in the compressed layer is about $2n_c$. The present analysis can be performed in the future for shorter and lower intensity laser pulses in order to study CSA in a configuration in which the target remains opaque to the laser pulse. Moreover, a shorter laser pulse allows us to avoid the creation of multiple shocks in the upstream region.
- The density and the shape of the upstream region define the number of protons that can be accelerated in the shock and allow to control the competition between CSA and TNSA. It has to present an exponential decreasing density profile in order to allow the shock to keep a constant velocity. The optimization of key parameters shows that the best results can be obtained with the delay of 1.4–1.5 ns between the ns and ps laser pulses with the ps laser parameters used in this study. However, in these configurations, the shock deceleration in that region tends to broaden the proton energy distribution. With the two ns laser beams tailoring, the rear side actually verifies this condition with a scale length of 5 μm up to $x = 700$ μm; after this limit, the density decreases smoothly over a distance of 300 μm. The shock slows down on this last part of the density profile and broadens the proton energy distribution.

The use of gas targets with our tailoring scheme is a promising way to create ion beams well-suited for applications. For the first time, acceleration of protons to high energies is predicted with realistic gas jet density profiles. To obtain higher proton energies ($\geq$100 MeV), higher intensity lasers are needed ($a_0 \simeq$ 10–20) and the density profile before the tailoring process is the key factor for suppressing the laser filamentation in the gas wings. Consequently, the compression factor of the gas jet density, duration of the laser pulse, and the focal spot size are the parameters that can be used for further optimization of the proton acceleration.

ACKNOWLEDGMENTS

We acknowledge the help of the SMILEI team on the PIC code Smilei, especially Michael Grech and Frederic Perez, Leo Esnault and Rachel NUTER from the CELIA team for his work on p2sat python module. The PIC simulation work was granted access to HPC resources of TGCC under the Allocation No. A0010506129 made by GENCI and under the Allocation No. 2020225390 of 60M CPU hours made by PRACE. This work has been carried out in the framework of regional Project No. POPRA2 supported by the New Aquitaine Regional Council (Convention No. 18003358). This work has received funding from the European Union's Horizon 2020 research and innovation program under Grant Agreement No. 871124 Laserlab-Europe.

AUTHORS DECLARATIONS

Conflict of Interest

The authors have no conflicts to disclose.

DATA AVAILABILITY

The data that support the findings of this study are available from the corresponding author upon reasonable request.

REFERENCES

[1]J.-R. Marquès, P. Loiseau, J. Bonvalet, M. Tarisien, E. d'Humières, J. Domange, F. Hannachi, L. Lancia, O. Larroche, P. Nicolaï, P. Puyuelo-Valdes, L. Romagnani, J. J. Santos, and V. Tikhonchuk, "Over-critical sharp-gradient plasma slab produced by the collision of laser-induced blast-waves in a gas jet: Application to high-energy proton acceleration," Phys. Plasmas **28**, 023103 (2021).
[2]S. Bulanov, T. Esirkepov, P. Migliozzi, F. Pegoraro, T. Tajima, and F. Terranova, "Neutrino oscillation studies with laser-driven beam dump facilities," Nucl. Instrum. Methods Res., Sect. A **540**, 25–41 (2005).
[3]G. A. Mourou, T. Tajima, and S. V. Bulanov, "Optics in the relativistic regime," Rev. Mod. Phys. **78**, 309–371 (2006).
[4]C. K. Li, F. H. Séguin, J. A. Frenje, J. R. Rygg, R. D. Petrasso, R. P. J. Town, P. A. Amendt, S. P. Hatchett, O. L. Landen, A. J. Mackinnon, P. K. Patel, V. A. Smalyuk, T. C. Sangster, and J. P. Knauer, "Measuring e and b fields in laser-produced plasmas with monoenergetic proton radiography," Phys. Rev. Lett. **97**, 135003 (2006).
[5]L. Romagnani, S. V. Bulanov, M. Borghesi, P. Audebert, J. C. Gauthier, K. Löwenbrück, A. J. Mackinnon, P. Patel, G. Pretzler, T. Toncian, and O. Willi, "Observation of collisionless shocks in laser-plasma experiments," Phys. Rev. Lett. **101**, 025004 (2008).
[6]S. Bulanov, T. Esirkepov, V. Khoroshkov, A. Kuznetsov, and F. Pegoraro, "Oncological hadrontherapy with laser ion accelerators," Phys. Lett. A **299**, 240–247 (2002).
[7]D. Schardt, "Tumor therapy with high-energy carbon ion beams," Nucl. Phys. A **787**, 633– 641 (2007).
[8]E. Lefebvre, E. D'Humières, S. Fritzler, and V. Malka, "Numerical simulation of isotope production for positron emission tomography with laser-accelerated ions," J. Appl. Phys. **100**, 113308 (2006).
[9]R. A. Snavely, M. H. Key, S. P. Hatchett, T. E. Cowan, M. Roth, T. W. Phillips, M. A. Stoyer, E. A. Henry, T. C. Sangster, M. S. Singh, S. C. Wilks, A. MacKinnon, A. Offenberger, D. M. Pennington, K. Yasuike, A. B. Langdon, B. F. Lasinski, J. Johnson, M. D. Perry, and E. M. Campbell, "Intense high-energy proton beams from petawatt-laser irradiation of solids," Phys. Rev. Lett. **85**, 2945–2948 (2000).
[10]S. Wilks, A. Langdon, T. Cowan, M. Roth, M. Singh, S. Hatchett, M. Key, D. Pennington, A. Mackinnon, and R. Snavely, "Energetic proton generation in ultra-intense laser-solid interactions," Phys. Plasmas **8**, 542–549 (2001).
[11]T. Esirkepov, M. Borghesi, S. V. Bulanov, G. Mourou, and T. Tajima, "Highly efficient relativistic-ion generation in the laser-piston regime," Phys. Rev. Lett. **92**, 175003 (2004).
[12]A. P. L. Robinson, M. Zepf, S. Kar, R. G. Evans, and C. Bellei, "Radiation pressure acceleration of thin foils with circularly polarized laser pulses," New J. Phys. **10**, 013021 (2008).

[13]A. Macchi, S. Veghini, and F. Pegoraro, "Light sail acceleration reexamined," Phys. Rev. Lett. **103**, 085003 (2009).
[14]B. Qiao, S. Kar, M. Geissler, P. Gibbon, M. Zepf, and M. Borghesi, "Dominance of radiation pressure in ion acceleration with linearly polarized pulses at intensities of 10^{21} W cm^{-2}," Phys. Rev. Lett. **108**, 115002 (2012).
[15]L. Yin, B. J. Albright, B. M. Hegelich, K. J. Bowers, K. A. Flippo, T. J. T. Kwan, and J. C. Fernández, "Monoenergetic ion acceleration from the laser breakout afterburner using ultrathin targets," Phys. Plasmas **14**, 056706 (2007).
[16]A. Henig, D. Kiefer, K. Markey, D. C. Gautier, K. A. Flippo, S. Letzring, R. P. Johnson, T. Shimada, L. Yin, B. J. Albright, K. J. Bowers, J. C. Fernández, S. G. Rykovanov, H.-C. Wu, M. Zepf, D. Jung, V. K. Liechtenstein, J. Schreiber, D. Habs, and B. M. Hegelich, "Enhanced laser-driven ion acceleration in the relativistic transparency regime," Phys. Rev. Lett. **103**, 045002 (2009).
[17]L. O. Silva, M. Marti, J. R. Davies, R. A. Fonseca, C. Ren, F. S. Tsung, and W. B. Mori, "Proton shock acceleration in laser-plasma interactions," Phys. Rev. Lett. **92**, 015002 (2004).
[18]F. Fiuza, A. Stockem, E. Boella, R. A. Fonseca, L. O. Silva, D. Haberberger, S. Tochitsky, W. B. Mori, and C. Joshi, "Ion acceleration from laser-driven electrostatic shocks," Phys. Plasmas **20**, 056304 (2013).
[19]E. Boella, F. Fiúza, A. S. Novo, R. Fonseca, and L. O. Silva, "Ion acceleration in electrostatic collisionless shock: On the optimal density profile for quasi-monoenergetic beams," Plasma Phys. Controlled Fusion **60**, 035010 (2018).
[20]C. A. J. Palmer, N. P. Dover, I. Pogorelsky, M. Babzien, G. I. Dudnikova, M. Ispiriyan, M. N. Polyanskiy, J. Schreiber, P. Shkolnikov, V. Yakimenko, and Z. Najmudin, "Monoenergetic proton beams accelerated by a radiation pressure driven shock," Phys. Rev. Lett. **106**, 014801 (2011).
[21]Y.-H. Chen, M. Helle, A. Ting, D. Gordon, N. Dover, O. Ettlinger, Z. Najmudin, M. Polyanskiy, I. Pogorelsky, and M. Babzien, "Laser acceleration of protons with an optically shaped, near-critical hydrogen gas target," AIP Conf. Proc. **1812**, 090002 (2017).
[22]S. Chen, M. Vranic, T. Gangolf, E. Boella, P. Antici, M. Bailly-Grandvaux, P. Loiseau, H. Pépin, G. Revet, J. Santos, A. Schroer, M. Starodubtsev, O. Willi, L. Silva, E. d'Humières, and J. Fuchs, "Collimated protons accelerated from an overdense gas jet irradiated by a 1 μm wavelength high-intensity short-pulse laser," Sci. Rep. **17**, 12910 (2017).
[23]P. Puyuelo-Valdes, J. L. Henares, F. Hannachi, T. Ceccotti, J. Domange, M. Ehret, E. d'Humieres, L. Lancia, J.-R. Marquès, X. Ribeyre, J. J. Santos, V. Tikhonchuk, and M. Tarisien, "Proton acceleration by collisionless shocks using a supersonic H_2 gas-jet target and high-power infrared laser pulses," Phys. Plasmas **26**, 123109 (2019).
[24]O. Tresca, N. P. Dover, N. Cook, C. Maharjan, M. N. Polyanskiy, Z. Najmudin, P. Shkolnikov, and I. Pogorelsky, "Spectral modification of shock accelerated ions using a hydrodynamically shaped gas target," Phys. Rev. Lett. **115**, 094802 (2015).
[25]A. Pak, S. Kerr, N. Lemos, A. Link, P. Patel, F. Albert, L. Divol, B. B. Pollock, D. Haberberger, D. Froula, M. Gauthier, S. H. Glenzer, A. Longman, L. Manzoor, R. Fedosejevs, S. Tochitsky, C. Joshi, and F. Fiuza, "Collisionless shock acceleration of narrow energy spread ion beams from mixed species plasmas using 1 μm lasers," Phys. Rev. Accel. Beams **21**, 103401 (2018).
[26]P. K. Singh, V. B. Pathak, J. H. Shin, I. W. Choi, K. Nakajima, S. K. Lee, J. H. Sung, H. W. Lee, Y. J. Rhee, C. Aniculaesei, C. M. Kim, K. H. Pae, M. H. Cho, C. Hojbota, S. G. Lee, F. Mollica, V. Malka, C.-M. Ryu, H. T. Kim, and C. H. Nam, "Electrostatic shock acceleration of ions in near-critical-density plasma driven by a femtosecond petawatt laser," Sci. Rep. **10**, 18452 (2020).
[27]E. Lefebvre, S. Bernard, C. Esnault, P. Gauthier, A. Grisollet, P. Hoch, L. Jacquet, G. Kluth, S. Laffite, S. Liberatore, I. Marmajou, P.-E. Masson-Laborde, O. Morice, and J.-L. Willien, "Development and validation of the TROLL radiation-hydrodynamics code for 3D hohlraum calculations," Nucl. Fusion **59**, 032010 (2018).
[28]J. Derouillat, A. Beck, F. Pérez, T. Vinci, M. Chiaramello, A. Grassi, M. Flé, G. Bouchard, I. Plotnikov, N. Aunai, J. Dargent, C. Riconda, and M. Grech, "Smilei: A collaborative, open-source, multi-purpose particle-in-cell code for plasma simulation," Comp. Phys. Commun. **222**, 351– 373 (2018).
[29]R. Z. Sagdeev, "Cooperative phenomena and shock waves in collisionless plasmas," Rev. Plasma Phys. **4**, 23 (1966).
[30]A. Macchi, A. S. Nindrayog, and F. Pegoraro, "Solitary versus shock wave acceleration in laser-plasma interactions," Phys. Rev. E **85**, 046402 (2012).
[31]E. D'Humières, P. Antici, M. Glesser, J. Boeker, F. Cardelli, S. Chen, J. Feugeas, F. Filippi, M. Gauthier, A. Levy, P. Nicolaï, H. Pépin, L. Romagnani, M. Scisciò, O. Willi, jc Kieffer, and J. Fuchs, "Investigation of laser ion acceleration in low-density targets using exploded foils," Plasma Phys. Controlled Fusion **55**, 124025 (2013).
[32]M. Gauthier, A. Lévy, E. d'Humières, M. Glesser, B. Albertazzi, C. Beaucourt, J. Breil, S. N. Chen, V. Dervieux, J. L. Feugeas, P. Nicolaï, V. Tikhonchuk, H. Pépin, P. Antici, and J. Fuchs, "Investigation of longitudinal proton acceleration in exploded targets irradiated by intense short-pulse laser," Phys. Plasmas **21**, 013102 (2014).
[33]P. Antici, E. Boella, S. Chen, D. Andrews, M. Barberio, J. Boeker, F. Cardelli, J. Feugeas, M. Glesser, P. Nicolaï, L. Romagnani, M. Scisciò, M. Starodubtsev, O. Willi, jc Kieffer, H. Pépin, L. Silva, E. D'Humières, and J. Fuchs, "Acceleration of collimated 45 MeV protons by collisionless shocks driven in low-density, large-scale gradient plasmas by a 10^{20} w/cm^2, 1 micron wavelength laser," Sci. Rep. **7**, 16463 (2017).
[34]T. Grismayer and P. Mora, "Influence of a finite initial ion density gradient on plasma expansion into a vacuum," Phys. Plasmas **13**, 032103 (2006).
[35]S. Tochitsky, A. Pak, F. Fiuza, D. Haberberger, N. Lemos, A. Link, D. H. Froula, and C. Joshi, "Laser-driven collisionless shock acceleration of ions from near-critical plasmas," Phys. Plasmas **27**, 083102 (2020).
[36]F. Sylla, A. Flacco, S. Kahaly, M. Veltcheva, A. Lifschitz, V. Malka, E. d'Humières, I. Andriyash, and V. Tikhonchuk, "Short intense laser pulse collapse in near-critical plasma," Phys. Rev. Lett. **110**, 085001 (2013).
[37]J. Marburger, "Self-focusing: Theory," Prog. Quantum Electron. **4**, 35–110 (1975).
[38]C. E. Max, J. Arons, and A. B. Langdon, "Self-modulation and self-focusing of electromagnetic waves in plasmas," Phys. Rev. Lett. **33**, 209–212 (1974).
[39]L. Willingale, S. P. D. Mangles, P. M. Nilson, R. J. Clarke, A. E. Dangor, M. C. Kaluza, S. Karsch, K. L. Lancaster, W. B. Mori, Z. Najmudin, J. Schreiber, A. G. R. Thomas, M. S. Wei, and K. Krushelnick, "Collimated multi-MeV ion beams from high-intensity laser interactions with underdense plasma," Phys. Rev. Lett. **96**, 245002 (2006).
[40]T. Nakamura, S. V. Bulanov, T. Z. Esirkepov, and M. Kando, "High-energy ions from near-critical density plasmas via magnetic vortex acceleration," Phys. Rev. Lett. **105**, 135002 (2010).